MATERIALS CHEMISTRY FRONTIERS

RESEARCH ARTICLE

View Article Online
View Journal | View Issue

Cite this: *Mater. Chem. Front.*, 2022, **6**, 333

Three birds with one stone: a single AIEgen for dual-organelle imaging, cell viability evaluation and photodynamic cancer cell ablation†

Yuewei Zhang,[ab] Shuohang Wang,[a] Ning Zhang,[a] Xiaodong Wang,[b] Qi Zan,[b] Li Fan,*[b] Xue Yu,*[a] Shaomin Shuang[b] and Chuan Dong*[b]

Received 15th September 2021,
Accepted 11th December 2021

DOI: 10.1039/d1qm01270c

rsc.li/frontiers-materials

Fully understanding the relationship among various organelles and cell viability is greatly important to clarify the mechanism of cancer diagnosis and treatment. However, the development of a single fluorescent probe capable of visualizing dual-organelles, cell viability and photodynamic therapy (PDT) of cancer cells is severely deficient. Herein, we rationally designed and presented a multifunctional aggregation-induced emission luminogen (AIEgen), **Mito-TTPE**, which first localized in mitochondria with near-infrared (NIR) fluorescence, and further was partially hydrolyzed by esterase, resulting in the accumulation of lipophilic and blue-emissive LD-TTP in lipid droplets. Owing to the distinct two-color emission and dual-organelle targeting changes tuned by esterase hydrolysis, **Mito-TTPE** was successfully used for evaluating cell viability. More importantly, the remarkable ROS generation ability of **Mito-TTPE** enabled the efficient photodynamic ablation of cancer cells.

Introduction

As the basic unit of life, cells are ingenious and complex chemical machines that perform a variety of biological activities. Various biological species within cells, including small biomolecules and macromolecules, cooperate to perform multiple biological functions.[1] For example, as one of the most important intracellular macromolecules, enzymes participate in a series of biochemical reactions necessary for normal life.[2] Meanwhile, the subcellular organelles that assembled with various biomolecules are also essential for various biological processes.[3] Amongst them, mitochondria as a double-membrane-bound organelle play important roles in cell metabolism, including energy supply for cell-life activities and cellular status regulation.[4–6] Lipid droplets (LDs), another important cytoplasmic organelle found in most eukaryotic cells, are involved in lipid metabolism, membrane formation, and energy generation and storage.[7–9] In particular, the interactions between various biological species and different organelles play a crucial role in significant biological events, such as the cellular apoptosis process. Previous research has shown that the execution of cell apoptosis starts from the sudden increase of mitochondrial membrane permeability, which would release harmful substances contained within the mitochondrial double-membrane into the cytoplasm, thereby triggering the apoptosis process.[10,11] Meanwhile, this process is inevitably accompanied by a decrease in enzymatic activity and cell viability, and lipid droplets can collect toxic acids to reduce inflammation.[12,13] Thus, the development of a facile approach for mitochondria/LD dual-imaging, cell viability evaluation and simultaneously cancer cell diagnosis and precise therapy is highly desirable and a critical challenge.

Fluorescence imaging techniques assisted with fluorescent probes have become a powerful tool because of their non-invasiveness, high sensitivity, and *in situ* and real-time visualization of biological species at subcellular levels. Currently, many probes have been developed for the imaging of intracellular active substances and/or single/double organelles.[14–29] However, because of the π–π stacking and other non-radiative pathways, conventional fluorophores often suffer from an aggregation-caused quenching (ACQ) effect, which might lead to weak fluorescence emission in the aggregation state and easy photobleaching. Fortunately, a new class of aggregation- induced emission (AIE) luminogens that was first proposed by Tang' group in 2001,[30] could perfectly solve the ACQ problems. The AIE luminogens (AIEgens) are non-emissive or faintly emissive in solution but emit intense fluorescence in the aggregated state due to the restriction of intramolecular motions (RIM).[30–33] Taking advantage of their intrinsic features, AIEgens usually display large Stokes shift, superior photostability and high sensitivity, which

[a] *School of Chemistry and Pharmaceutical Engineering, Jilin Institute of Chemical Technology, Jilin, 132022, P. R. China*
[b] *Institute of Environmental Science, Shanxi Laboratory for Yellow River, College of Chemistry and Chemical Engineering, Shanxi University, Taiyuan, 030006, P. R. China. E-mail: fanli128@sxu.edu.cn, dongjibinghuayuxue@163.com, dc@sxu.edu.cn*

† Electronic supplementary information (ESI) available. See DOI: 10.1039/d1qm01270c

endow them with promising potential for monitoring of bioactive substances like esterase activity in living systems. For example, Li *et al.* reported an AIEgen-based bioprobe (DEAM) through integration with an esterase recognizable acetoxyl unit for sensing intracellular esterase activity.[34] By the conjugation of an AIEgen with cationic and hydrolyzable moieties, a single AIEgen named TVQE was developed for imaging of dual-organelles and evaluation of cell viability.[35] In addition, recent evidence demonstrated that some AIEgens could also generate reactive oxygen species (ROS) in the aggregation state upon light irradiation, making them effective photosensitizers for photodynamic therapy (PDT).[36–40] For instance, Tang *et al.* rationally constructed a H_2O_2-responsive AIE probe TTPy–H_2O_2 for imaging-guided organelle targeting and photodynamic cancer cell ablation.[38] Wang *et al.* reported a LD-targeted and AIE-active photosensitizer TPECNPB for H_2O_2-activatable fluorescence-guided PDT on cancer cells.[39] Zhao *et al.* developed an esterase-responsive prodrug (TPEQC) by conjugating an anticancer drug of chlorambucil with an AIE active photosensitizer for lysosome/mitochondria dual-targeted and image-guided cancer therapy through synergetic chemo-photodynamic cancer therapy.[40] However, a single AIEgen that is capable of the dual-imaging of mitochondria/lipid droplets, detection of cell viability and simultaneously PDT on cancer cells has rarely been reported.

In view of the above situation, herein, we fabricated an esterase-sensitive AIE probe for dual-organelle imaging, viability evaluation and photodynamic cancer cell ablation for the first time. As demonstrated in Scheme 1, **Mito-TTPE** contains a pyridinium cationic moiety with a potential of 6.35 mV (Fig. S1, ESI†), which could target mitochondria through electrostatic interactions with the electronegative mitochondrial membrane.[38,41] An acetoxy group was chosen as the esterase activatable site, which was predicted to reflect cell viability through esterase activity changes.[35,42] Meanwhile, the hydrolyzed product LD-TTP with *C* log *P* of 6.698 has been reported as a superior LD-specific probe.[43] In addition, the electron-accepting pyridinium cation was linked to a triphenylamine-thiophene segment, forming a twisted donor–acceptor (D–A) structure that facilitates red-shift, the fluorescence to the NIR emission region and large Stokes shift. Furthermore, the multiple freely rotatable phenyl groups and double bond help to quench the fluorescence in the solution, while displaying AIE within the targeted organelle.[38,44] More importantly, it has been reported that this strong D–A structure usually exhibited great potential as a good photosensitizer for PDT.[45,46] Based on the above design strategy, we have successfully synthesized **Mito-TTPE** (Scheme 1 and Scheme S1, ESI†), an AIE probe first targeted to mitochondria with NIR fluorescence. After being hydrolyzed by mitochondrial esterase in living cells, **Mito-TTPE** was partially transformed into a blue-emissive LD-TTP, which could specifically accumulate in LDs. Due to this distinct two-color emission and dual-organelle targeting changes regulated by esterase hydrolysis, **Mito-TTPE** was successfully used for evaluating cell viability. More interestingly, **Mito-TTPE** has been applied as an indicator for efficient PDT on cancer cells.

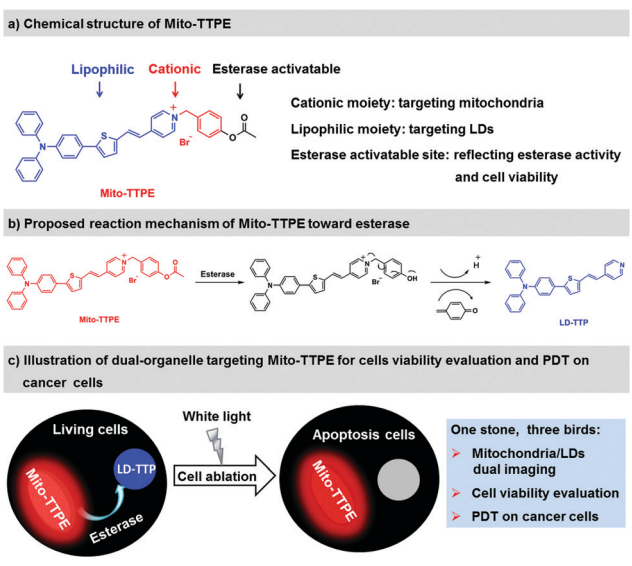

Scheme 1 (a) Chemical structure of **Mito-TTPE**. (b) Propose reaction mechanism of **Mito-TTPE** towards esterase. (c) Illustration of dual-organelle targeting of **Mito-TTPE** for cell viability evaluation and PDT on cancer cells.

Experimental section

Materials and apparatus

4-(Bromomethyl)phenyl acetate, human carboxylesterase 2 (CES2), 9,10-anthracenediyl-bis(methylene)dimalonic acid (ABDA) and 2′,7′-dichlorodihydrofluorescein diacetate (DCFH-DA) were commercially available from Sigma-Aldrich. Mito-Tracker Green (MTG) and Nile Red were obtained from Thermo Fisher Scientific. A calcein-AM/PI kit was purchased from Solarbio. All other solvents were bought from Tianjin Damao Chemical Reagent Factory, and used without further purification unless otherwise specified.

NMR spectra were determined with a Bruker instrument at 600 MHz for ^{1}H NMR and 150 MHz for ^{13}C NMR, respectively. High-resolution mass spectrometric (HR-MS) data were acquired on an Agilent Accurate-Mass-Q-TOF MS 6520 system. UV-vis absorption spectra were measured on a TU-1901 double-beam UV-vis spectrophotometer. Fluorescence spectra were measured on an FLS-920 Edinburgh Fluorescence Spectrophotometer. Fluorescence images were collected on a confocal laser scanning microscope (CLSM) (Zeiss, LSM880).

Synthesis of Mito-TTPE

LD-TTP (50 mg, 0.12 mmol) and 4-(bromomethyl)phenyl acetate (55 mg, 0.24 mmol) were refluxed in anhydrous toluene (2.5 mL) overnight under argon. After cooling to room temperature, the solvent was removed under reduced pressure, and the residue was purified by silica chromatography using CH_2Cl_2/MeOH = 30 : 1 (v/v) to give **Mito-TTPE** as a purple solid (72 mg, 78%). ^{1}H NMR (600 MHz, DMSO-d_6) δ 9.03 (s, J = 6.0 Hz, 2H, pyridyl-H), 8.23 (d, J = 16.8 Hz, 1H, HC═CH), 8.21 (d, J = 4.8 Hz, 2H, pyridyl-H), 7.62–7.63 (d, 2H, phenyl-H), 7.59–7.58 (d, 2H, phenyl-H), 7.51 (s, 2H, thienyl-H), 7.35–7.34 (m, 4H, phenyl-H), 7.23–7.21 (d, J = 8.4 Hz, 2H, phenyl-H), 7.15–7.08 (m, 6H, phenyl-H), 7.12 (d, J = 16.8 Hz, 1H, HC═CH) 6.98–6.97

(d, J = 8.4 Hz, 2H, phenyl-H), 5.72 (s, 2H, CH_2), 2.27 (s, 3H, CH_3). ^{13}C NMR (150 MHz, DMSO-d_6) δ 169.60, 153.54, 151.49, 148.33, 147.98, 147.00, 144.48, 139.12, 134.89, 134.53, 132.64, 130.43, 130.24, 127.32, 126.68, 125.27, 124.41, 124.09, 123.13, 122.60, 121.61, 61.89, 21.31. HR-MS m/z: $[M + H]^+$ calculated for $C_{38}H_{31}N_2O_2S^+$, 579.2101; measured, 579.2099.

Optical properties of Mito-TTPE

Mito-TTPE was dissolved in DMSO to prepare the stock solution (1.0 mM). The AIE properties of **Mito-TTPE** (5 μM) were investigated in EtOH/hexane mixtures with various hexane fractions. The spectra of **Mito-TTPE** (2 μM) with carboxylesterase 2 (CES2, 2 μg mL^{-1}) were tested in PBS (pH 7.4) at different times. The singlet oxygen ($^1O_2$) and total ROS generation capability of **Mito-TTPE** (10 μM) or LD-TTP (10 μM) were monitored by UV/vis spectroscopy of ABDA (100 μM) and fluorescence spectroscopy of dichlorofluorescin (DCFH, 10 μM), respectively, under white light irradiation (1.75 mW cm^{-2}).

Cell culture and cytotoxicity assay

The cell culture and cell cytotoxicity assay of **Mito-TTPE** and LD-TTP on HeLa cells were listed in the ESI.†

Colocalization experiments

HeLa cells were co-incubated with **Mito-TTPE** or LD-TTP (5 μM) and MTG (1 μM) or Nile Red (0.3 μM) for 30 min, respectively. The fluorescence images were captured using a CLSM. **Mito-TTPE** in the red channel: λ_{ex} = 488 nm, λ_{em} = 600–710 nm; MTG: λ_{ex} = 488 nm, λ_{em} = 495–540 nm; Nile red: λ_{ex} = 561 nm, λ_{em} = 600–670 nm; **Mito-TTPE** in the blue channel or LD-TTP: λ_{ex} = 405 nm, λ_{em} = 540–600 nm.

Evaluation of cell viability

For living cells: living HeLa cells were stained with **Mito-TTPE** (5 μM) for 30 min. For early apoptotic cells: after being pretreated with H_2O_2 (10 mM) for 1 h, living HeLa cells were then incubated with **Mito-TTPE** (5 μM) for another 30 min. For late apoptotic cells: after being pretreated with H_2O_2 (10 mM) for 5 h, living HeLa cells were then incubated with **Mito-TTPE** (5 μM) for another 40 min. For dead cells: living HeLa cells were first treated with paraformaldehyde (4%) for 30 min, then incubated with **Mito-TTPE** (5 μM) for a further 30 min. The fluorescence images were captured using a CLSM in the blue channel (λ_{ex} = 405 nm, λ_{em} = 540–600 nm) for hydrolysate LD-TTP and red channel (λ_{ex} = 488 nm, λ_{em} = 600–710 nm) for **Mito-TTPE**, respectively.

Intracellular ROS detection

HeLa cells were first treated with DCFH-DA (10 μM) for 1 h, then incubated with **Mito-TTPE** (5 μM) for another 30 min. The fluorescence images were captured using a CLSM in the green channel (λ_{ex} = 488 nm, λ_{em} = 500–550 nm) for DCFH-DA.

Cytotoxicity assay by calcein-AM/PI kit

A Calcein-AM/PI kit was used to analyze the cell viability and morphology of HeLa cells. For H_2O_2-induced cells apoptosis: after being treated with H_2O_2 (10 μM) for 4.5 h, HeLa cells were incubated with **Mito-TTPE** (5 μM) for 30 min. Then calcein-AM (0.67 μM)/PI (1.5 μM) was used to stain the HeLa cells for another 30 min. For cell apoptosis induced by white light irradiation: after being incubated with **Mito-TTPE** (5 μM) for 30 min, HeLa cells were treated with or without light irradiation (50 mW cm^{-2}) for 30 min. Then calcein-AM (0.67 μM)/PI (1.5 μM) was used to stain the HeLa cells for another 30 min. The fluorescence images were captured using a CLSM in the green channel (λ_{ex} = 488 nm, λ_{em} = 500–550 nm) for calcein-AM and red channel (λ_{ex} = 561 nm, λ_{em} = 630–700 nm) for PI.

Results and discussion

Synthesis and characterization of Mito-TTPE

Mito-TTPE was facilely synthesized by a substitution reaction between LD-TTP and 4-(bromomethyl)phenyl acetate, as listed in Scheme S1 in the ESI.† LD-TTP was synthesized according to our reported literature,[43] and was also the product in response to human carboxylesterase 2 (CES2, which is majorly expressed in the intestines for hydrolysis of esters, amides and thioesters). **Mito-TTPE** was prepared in good yield and fully characterized by NMR spectroscopy and high-resolution mass spectrometry (HR-MS) (ESI†).

Photophysical properties

First, the AIE feature of **Mito-TTPE** was investigated in EtOH/hexane mixtures with increasing hexane fractions (f_H). As depicted in Fig. 1a, **Mito-TTPE** exhibited faint emission in 100% EtOH, while when f_H was higher than 60%, the fluorescence intensity increased rapidly with a hypochromic shift from 712 nm to 646 nm. The strongest fluorescence intensity was observed at a f_H of 95% with $\alpha_{AIE}(I/I_0)$ about 28 (Fig. 1b), suggesting typical AIE characteristics. Dynamic light scattering (DLS) analysis further verified the nanoaggregate formation, with an average hydrodynamic diameter of 186.9 nm (Fig. S2a, ESI†). Moreover, the solid-state fluorescence emission was peaked at about 714 nm (Fig. S2b, ESI†), displaying near-infrared (NIR)-emissive AIE behaviour.

To verify whether **Mito-TTPE** was responsive to esterase as designed, the optical properties of **Mito-TTPE** were measured in the absence and presence of CES2, in PBS (pH 7.4) at room temperature. Fig. 1c and d depict the fluorescence spectra of **Mito-TTPE** reacting with CES2. In the absence of CES2, only a maximum emission around 660 nm was observed (Fig. 1c). With the extension of the reaction time, the emission reduced gradually, accompanied by a significantly enhanced fluorescence emission with a peak around 550 nm (Fig. 1d), which was in accordance with the fluorescence spectra of LD-TTP in PBS,[43] indicating that **Mito-TTPE** could be hydrolyzed to LD-TTP by active esterase. Notably, there was an about 140 nm emission shift between the emission peak of **Mito-TTPE** and LD-TTP, which was favorable for the use of **Mito-TTPE** in dual-imaging in the red channel and blue channel. In addition, **Mito-TTPE** was highly selective toward CES2 over other biological analytes

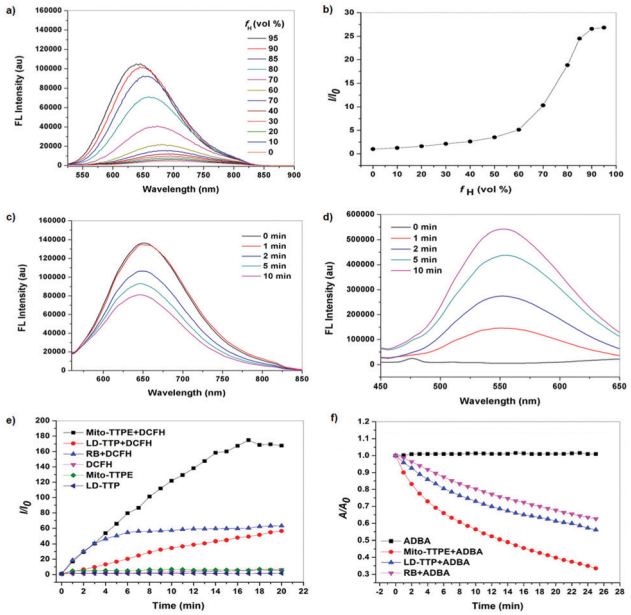

Fig. 1 (a) Fluorescence spectra of **Mito-TTPE** (5 μM) in EtOH/hexane mixtures with increasing hexane fractions (f_H) from 0% to 95%. λ_{ex} = 488 nm. (b) Plot of relative FL emission intensity (I/I_0) *versus* f_H. FL spectra of **Mito-TTPE** (2 μM) with CES2 (2 μg mL^{-1}) at different times with λ_{ex} = 495 nm (c) and λ_{ex} = 410 nm (d) at 25 °C. (e) Total ROS generation of **Mito-TTPE** (10 μM), LD-TTP (10 μM) and RB (10 μM) upon white light irradiation (1.75 mW cm^{-2}) using DCFH as an indicator. (f) Singlet oxygen ($^1O_2$) generation of **Mito-TTPE** (10 μM), LD-TTP (10 μM) and RB (10 μM) upon white light irradiation (1.75 mW cm^{-2}) using ABDA (100 μM) as an indicator.

(Fig. S3, ESI†), ensuring that the release of LD-TTP is specific for CES2-triggered probe activation.

In order to confirm the response mechanism of **Mito-TTPE** toward CES2 as proposed in Scheme 1, HR-MS analysis was conducted as shown in Fig. S4 (ESI†). Upon reaction with CES2, the mass peak of free **Mito-TTPE** at a peak of m/z = 579.2099 ([**Mito-TTPE**]$^+$, calcd: 579.2101) was no longer observed, while a new peak of m/z = 430.6963 corresponding to the formation of adduct ([**Mito-TTPB**-CES2]$^+$) was trapped, in agreement with LD-TTP ([LD-TTP]$^+$, calcd: 430.1504). Thus, the results further verified the design strategy illustrated in Scheme 1.

ROS generation ability of Mito-TTPE and LD-TTP

The efficiency of ROS generation of a photosensitizer (PS) upon light irradiation plays an important role in PDT. Thus, we first evaluated the total content of all kinds of ROS generation ability of **Mito-TTPE** and LD-TTP by monitoring the enhanced fluorescence intensity of dichlorofluorescin (DCFH) at 525 nm. As shown in Fig. 1e and Fig. S5 (ESI†), with increasing white light irradiation time, the fluorescence intensity of DCFH rapidly raised in the presence of **Mito-TTPE** and LD-TTP, reaching 167- and 56-fold enhancement within 20 min, thereby suggesting a high-efficiency ROS generation of **Mito-TTPE** and LD-TTP. Meanwhile, the singlet oxygen ($^1O_2$) generation from **Mito-TTPE** and LD-TTP was further evaluated by measuring the absorption of the photodegradation rate of 9,10-anthracenediyl-bis(methylene)dimalonic acid (ABDA). As expected, the absorption intensity of ABDA at about 419 nm decreased gradually upon white light irradiation in the presence of **Mito-TTPE** and LD-TTP, while almost no obvious degradation was observed without PSs, indicating that **Mito-TTPE** and LD-TTP can generate ROS efficiently to consume ABDA. Most importantly, **Mito-TTPE** was more powerful for ROS production, even outperforming commercial photosensitizer Rose Bengal (RB) (Fig. 1e and f). The results further demonstrated the remarkable ROS generation ability of **Mito-TTPE**.

Organelle-targeting ability of Mito-TTPE

Based on the above design strategy, **Mito-TTPE** containing a cationic moiety first tends to accumulate into mitochondria due to the electrostatic interaction between the cationic moiety and the mitochondrial negative membrane potential. Meanwhile, it can be hydrolyzed by intracellular carboxylesterases 2 (CES2) to compound LD-TTP, which has excellent lipid droplet targeting ability.[43] We speculated that both red fluorescence from **Mito-TTPE** and blue fluorescence from the hydrolyzed product LD-TTP could be observed in living cells.

To confirm this speculation, living HeLa cells were incubated with **Mito-TTPE** and LD-TTP, respectively, and observed in the dual-channel imaging mode (red and blue channels). As expected, **Mito-TTPE** exhibited obvious fluorescence emissions in both the red and blue channels (Fig. 2a–c), while only blue fluorescent signals were detected in the LD-TTP-stained cells (Fig. 2e–g). Moreover, in the red channel of **Mito-TTPE**, a clear and typical mitochondrial filamentous structure was observed, and in the both blue channel of **Mito-TTPE** and LD-TTP, the spherical spot morphologies of LDs were observed (Fig. 2d and e). These phenomena suggested that the red-emissive **Mito-TTPE** could be hydrolyzed into LD-TTP with blue emission in living cells.

To further verify the subcellular location of **Mito-TTPE**, co-localization imaging experiments with commercial mitochondria staining dye MTG and LD staining dye Nile Red were performed, respectively. As expected, the red fluorescence emission of **Mito-TTPE** overlapped well with that of MTG with a high Pearson's co-localization coefficient of 0.93 (Fig. 3a–d); similarly, the blue fluorescence signal from **Mito-TTPE** showed

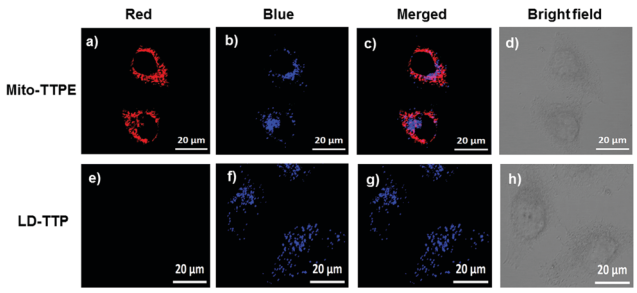

Fig. 2 Fluorescence images of living HeLa cells stained with 5 μM **Mito-TTPE** and 5 μM LD-TTP in the red channel: λ_{ex} = 488 nm, λ_{em} = 600–710 nm (a and e), and blue channel: λ_{ex} = 405 nm, λ_{em} = 540–600 nm (b and f), respectively. (c and g) Merged image. (d and h) Bright-field image. Scale bar: 20 μm.

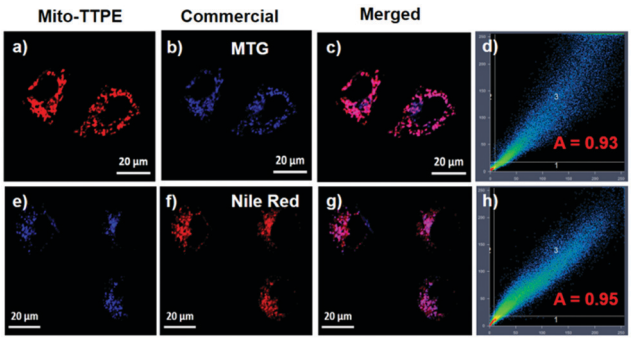

Fig. 3 Fluorescence images of living HeLa cells co-stained with 5 μM **Mito-TTPE** (a and e) and 1 μM MTG (b) or 0.3 μM Nile Red (f), respectively. (c and g) Merged image. (d and h) Bright-field image. **Mito-TTPE** in the red channel: λ_{ex} = 488 nm, λ_{em} = 600–710 nm; **Mito-TTPE** in the blue channel: λ_{ex} = 405 nm, λ_{em} = 540–600 nm; MTG: λ_{ex} = 488 nm, λ_{em} = 495–540 nm; Nile Red: λ_{ex} = 561 nm, λ_{em} = 600–670 nm. Scale bar: 20 μm.

excellent overlap with that of Nile Red (Pearson's colocalization coefficient of 0.95) (Fig. 3e–h).

The results indicated that **Mito-TTPE** was a mitochondria-targeting probe with red emission, while the hydrolysate **LD-TTP** could specifically locate in LDs as per the previous report.[38,43]

Then, the real-time and *in situ* imaging performance of **Mito-TTPE** was investigated in living HeLa cells and A549 cells, respectively. As shown in Fig. 4 and Fig. S6 (ESI†), **Mito-TTPE** first stained mitochondria and emitted red fluorescence; about 20 minutes later, the lipid droplets in the blue channel are also specifically lit in both living HeLa and A549 cells. It should be noted that the fluorescence intensity in the red channel reached the maximum at about 30 min in living HeLa cells and 40 min in living A549 cells, respectively, and then both decreased gradually. Meanwhile, the fluorescence in the blue channel increased with increased time. The results demonstrated that **Mito-TTPE** exclusively stained mitochondria owing to the electrostatic interaction in living cells, and furthermore was hydrolyzed to the lipophilic hydrolysate by intracellular carboxylesterases, which could gradually accumulate in LDs.

Evaluation of cell viability using Mito-TTPE

Since esterase activity can reflect cell viability, we studied whether **Mito-TTPE** can be used to assess cell viability. The dual-channel imaging experiments were performed in living, early apoptosis, late apoptosis and dead HeLa cells, respectively. Because of the high activity of esterase in living cells, the fluorescence emission signals in both the blue and red channels were clear in the **Mito-TTPE**-stained living cells (Fig. 5), demonstrating that **Mito-TTPE** was partially hydrolyzed into LD-TTP by active esterase. It is known that overexpression of reactive oxygen species (ROS) such as H_2O_2 could lead to the imbalance of the redox state in cells, eventually triggering cell apoptosis,[38,39] during which the esterase activity is reduced. Then, HeLa cells were treated with H_2O_2 for 1 h and 5 h, respectively, and early and late apoptotic cells could be clearly and differentially visualized using **Mito-TTPE**. As revealed in Fig. 5, the blue fluorescence signals in the late apoptotic cells were weaker than those from the early apoptotic cells. In particular, owing to the inactivated esterase activity in dead cells, it is difficult to collect the blue fluorescence signals, but strong red emission can be detected in the **Mito-TTPE**-stained dead HeLa cells. The data indicated that **Mito-TTPE** can

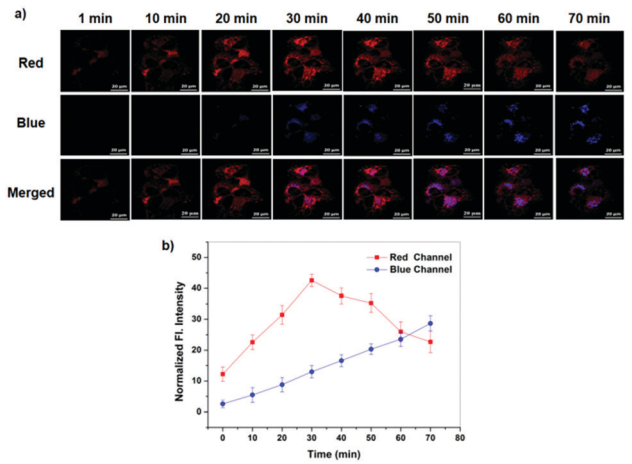

Fig. 4 (a) Time-dependent fluorescence images of living HeLa cells stained with 5 μM **Mito-TTPE**. Red channel: λ_{ex} = 488 nm, λ_{em} = 600–710 nm; blue channel: λ_{ex} = 405 nm, λ_{em} = 540–600 nm. Scale bar: 20 μm. (b) FL intensity changes in the red and blue channel in living HeLa cells incubated with **Mito-TTPE** at different time points (±S.D., n = 3).

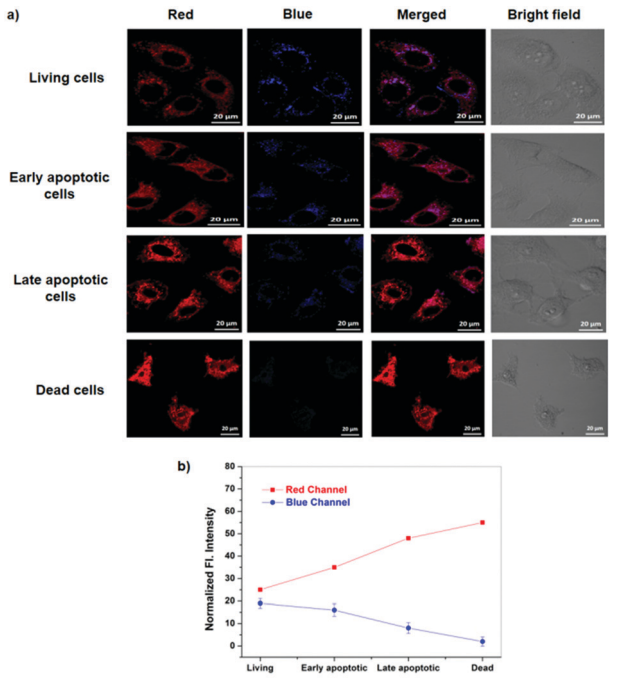

Fig. 5 (a) Fluorescence images of living, early apoptotic, late apoptotic and dead HeLa cells stained with 5 μM **Mito-TTPE**. Red channel: λ_{ex} = 488 nm, λ_{em} = 600–710 nm; blue channel: λ_{ex} = 405 nm, λ_{em} = 540–600 nm. Scale bar: 20 μm. (b) Normalized fluorescence intensity obtained from a (±S.D., n = 3).

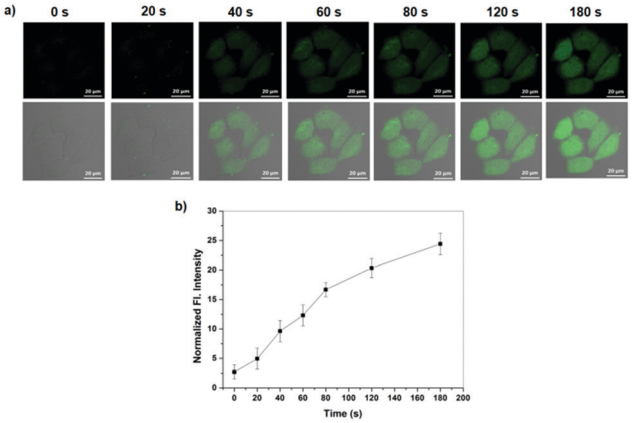

Fig. 6 (a) Intracellular ROS level using DCFH-DA as an indicator in living HeLa cells stained with 5 μM **Mito-TTPE** under white light irradiation (50 mW cm^{-2}) for different times. DCFH-DA: λ_{ex} = 488 nm, λ_{em} = 500–550 nm. Scale bar: 20 μm. (b) Normalized fluorescence intensity obtained from a (±S.D., n = 3).

effectively evaluate different cell viabilities with different fluorescence intensity changes of the dual-channel in living, early apoptosis, late apoptosis and dead cells. Furthermore, the results were in agreement with the evaluation of cell viability using an EdU assay (Fig. S7, ESI†).

Intracellular ROS detection and PDT ablation of cancer cells

With the explicit indications of dual-organelle imaging and excellent ROS generation ability *in vitro* confirmed, **Mito-TTPE** was studied for its ROS generation ability inside cells using 2′,7′-dichlorodi-hydrofluorescein diacetate (DCFH-DA, a non-emissive dye that can be de-esterified intracellularly and turn to highly emissive DCFH upon ROS oxidation) as the ROS fluorescence indicator. After incubating with **Mito-TTPE** for 30 min, living HeLa cells were treated with DCFH-DA for monitoring the intracellular ROS, which could be generated by both **Mito-TTPE** in the mitochondria and LD-TTP within LDs. As depicted in Fig. S8 (ESI†), control cells without **Mito-TTPE** displayed negligible emission; in contrast, an obvious fluorescence enhancement was observed along with increasing irradiation time in the presence of DCFH-DA (Fig. 6), suggesting effective ROS generation from **Mito-TTPE** in living cells upon light irradiation.

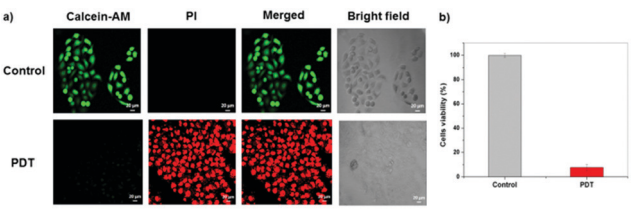

Fig. 7 (a) Fluorescence imaging of PDT of HeLa cells. Fluorescence imaging of HeLa cells stained with calcein-AM/PI after incubation with 5 μM **Mito-TTPE**, upon white light irradiation (50 mW cm^{-2}, 30 min). Green channel (λ_{ex} = 488 nm, λ_{em} = 500–550 nm) for calcein-AM; red channel (λ_{ex} = 561 nm, λ_{em} = 630–700 nm) for PI. Scale bar: 20 μm. (b) Viability of HeLa cells incubated with **Mito-TTPE** in the dark and under white light irradiation (50 mW cm^{-2}) for 30 min.

The efficient ROS generation by **Mito-TTPE** prompted us to investigate the PDT ablation of cancer cells *via* live/dead cell staining assay. Herein, after incubated with **Mito-TTPE** for 30 min, living HeLa cells were then treated with calcein-AM (green fluorescence for living cells)/PI (red fluorescence for dead cells) for a further 15 min. As shown in Fig. 7a, before light irradiation, the control cells exhibited a green calcein-AM signal, indicating the good biocompatibility of both **Mito-TTPE** and LD-TTP in the dark. However, after light irradiation for 30 min, bright red emission of PI was observed and almost no fluorescence was detected in the green channel, demonstrating the efficient PDT ablation of cancer cells, which has been confirmed by MTT assay (Fig. 7b). The results indicated that **Mito-TTPE** was an effective photosensitizer in PDT.

In addition, the cell viability of **Mito-TTPE** and LD-TTP was further confirmed in HeLa cells through the MTT assay. In dark conditions, both **Mito-TTPE** and LD-TTP exhibited relatively low cytotoxicity (Fig. S9, ESI†), implying their good biocompatibility. In contrast, upon white light irradiation, an obvious dose-dependent cytotoxicity was observed, after 30 min irradiation, only 20% and 30% of cell viability remained in the presence of 10 μM of **Mito-TTPE** and LD-TTP, respectively. These results indicated that both **Mito-TTPE** and LD-TTP were powerful for PDT of cancer cells, and **Mito-TTPE** exhibited more effective therapeutic output than LD-TTP, which was in agreement with the ROS generation ability in Fig. 1e and f.

Conclusion

In summary, we have constructed a versatile AIEgen, **Mito-TTPE**, bearing a lipophilic triphenylamine segment, and pyridinium cationic and esterase hydrolysis groups. Due to the hydrolysis of esterase in living cells, **Mito-TTPE** was able to selectively stain mitochondria and lipid droplets with NIR and blue fluorescence, respectively. Since the apoptosis process was usually accompanied by a decrease in esterase activity, living, apoptotic and dead cells could be visually distinguished using **Mito-TTPE** by monitoring the distinct two-color emission and dual-organelle targeting changes, suggesting its excellent cell viability evaluation ability. Noteworthily, **Mito-TTPE** also exhibited prominent ROS generation ability upon white light irradiation, which has been successfully used for efficient PDT of cancer cells. Therefore, **Mito-TTPE** shows great potential for both real-time monitoring of cell apoptosis and photodynamic ablation of cancer cells.

Conflicts of interest

There are no conflicts of interest to declare.

Acknowledgements

This work was supported by the National Natural Science Foundation of China (81901814 and 21874087), Science and Technology Project of Jilin Provincial Department of Education

(JJKH20200242KJ), Science and Technology Innovation and Development Plan Project in Jilin City (20190104196) and Research projects in Jilin Institute of Chemical Technology (2016004 and 2018030).

Notes and references

1 G. Bao and S. Suresh, Cell and molecular mechanics of biological materials, *Nat. Mater.*, 2003, **2**, 715–725.
2 D. Davidi, L. M. Longo, J. Jabłońska, R. Milo and D. S. Tawfik, A bird's-eye view of enzyme evolution: chemical, physicochemical, and physiological considerations, *Chem. Rev.*, 2018, **118**, 8786–8797.
3 S. Cohen, A. M. Valm and J. Lippincott-Schwartz, Interacting organelles, *Curr. Opin. Cell Biol.*, 2018, **53**, 84–91.
4 V. Gogvadze, S. Orrenius and B. Zhivotovsky, Mitochondria in cancer cells: what is so special about them?, *Trends Cell Biol.*, 2008, **18**, 165–173.
5 N. Zamzami and G. Kroemer, The mitochondrion in apoptosis: how Pandora & rsquos box opens, *Nat. Rev. Mol. Cell Biol.*, 2001, **2**, 67–71.
6 S. W. Tait and D. R. Green, Mitochondria and cell death: outer membrane permeabilization and beyond, *Nat. Rev. Mol. Cell Biol.*, 2010, **11**, 621–632.
7 F. Wilfling, J. T. Haas, T. C. Walther and R. V. Farese Jr, Lipid droplet biogenesis, *Curr. Opin. Cell Biol.*, 2014, **29**, 39–45.
8 Y. Guo, T. C. Walther, M. Rao, N. Stuurman, G. Goshima, K. Terayama, J. S. Wong, R. D. Vale, P. Walter and R. V. Farese, Functional genomic screen reveals genes involved in lipid-droplet formation and utilization, *Nature*, 2008, **453**, 657–661.
9 R. V. Farese and T. C. Walther, Lipid droplets finally get a little R-E-S-P-E-C-T, *Cell*, 2009, **139**, 855–860.
10 D. R. Green and J. C. Reed, Mitochondria and apoptosis, *Science*, 1998, **281**, 1309–1312.
11 M. G. Tian, J. Sun, B. L. Dong and W. Y. Lin, Dynamically monitoring cell viability in a dual-color mode: construction of an aggregation/monomer-based probe capable of reversible mitochondria-nucleus migration, *Angew. Chem., Int. Ed.*, 2018, **57**, 16506–16510.
12 R. S. Bell, L. A. Bourret, D. F. Bell, M. C. Gebhardt, A. Rosenberg, H. B. Berrey, B. V. Treadwell, W. W. Tomford and H. J. Mankin, Evaluation of fluorescein diacetate for flow cytometric determination of cell viability in orthopaedic research, *J. Orthop. Res.*, 1988, **6**, 467–474.
13 J. Boren and K. M. Brindle, Apoptosis-induced mitochondrial dysfunction causes cytoplasmic lipid droplet formation, *Cell Death Differ.*, 2012, **19**, 1561–1570.
14 W. Xu, Z. Zeng, J. H. Jiang, Y. T. Chang and L. Yuan, Discerning the chemistry in individual organelles with small-molecule fluorescent probes, *Angew. Chem., Int. Ed.*, 2016, **55**, 13658–13699.
15 Z. Yang, A. Sharma, J. Qi, X. Peng, D. Y. Lee, R. Hu, D. Lin, J. Qu and J. S. Kim, Super-resolution fluorescent materials: an insight into design and bioimaging applications, *Chem. Soc. Rev.*, 2016, **45**, 4651–4667.
16 P. Gao, W. Pan, N. Li and B. Tang, Fluorescent probes for organelle-targeted bioactive species imaging, *Chem. Sci.*, 2019, **10**, 6035–6071.
17 H. Zhu, J. L. Fan, J. J. Du and X. J. Peng, Fluorescent probes for sensing and imaging within specific cellular organelles, *Acc. Chem. Res.*, 2016, **49**, 2115–2126.
18 J. L. Kolanowski, F. Liu and E. J. New, Fluorescent probes for the simultaneous detection of multiple analytes in biology, *Chem. Soc. Rev.*, 2018, **47**, 195–208.
19 H. H. Han, H. Tian, Y. Zang, A. C. Sedgwick, J. Li, J. L. Sessler, X. P. He and T. D. James, Small-molecule fluorescence-based probes for interrogating major organ diseases, *Chem. Soc. Rev.*, 2021, **50**, 9391–9429, DOI: 10.1039/d0cs01183e.
20 M. T. Ye, W. Hu, M. He, C. C. Li, S. Y. Zhai, Z. H. Liu, Y. Y. Wang, H. J. Zhang and C. Y. Li, Deep imaging for visualizing nitric oxide in lipid droplets: discovering the relationship between nitric oxide and resistance to cancer chemotherapy drugs, *Chem. Commun.*, 2020, **56**, 6233–6236.
21 D. Bratosin, L. Mitrofan, C. Palii, J. Estaquier and J. Montreuil, Novel fluorescence assay using calcein-AM for the determination of human erythrocyte viability and aging, *Cytometry, Part A*, 2005, **66**, 78–84.
22 L. F. Guo, M. G. Tian, Z. Y. Zhang, Q. Lu, Z. Q. Liu, G. L. Niu and X. Q. Yu, Simultaneous two-color visualization of lipid droplets and endoplasmic reticulum and their interplay by single fluorescent probes in lambda mode, *J. Am. Chem. Soc.*, 2021, **143**, 3169–3179.
23 L. Fan, Q. Zan, X. D. Wang, S. H. Wang, Y. W. Zhang, W. J. Dong, S. M. Shuang and C. Dong, A mitochondria-specific orange/near-infrared-emissive fluorescent probe for dual-imaging of viscosity and H_2O_2 in inflammation and tumor models., *Chin. J. Chem.*, 2021, **39**, 1303–1309.
24 M. Collot, T. K. Fam, P. Ashokkumar, O. Faklaris, T. Galli, L. Danglot and A. S. Klymchenko, Ultrabright and fluorogenic probes for multicolor imaging and tracking of lipid droplets in cells and tissues, *J. Am. Chem. Soc.*, 2018, **140**, 5401–5411.
25 X. L. Xie, F. Y. Tang, G. Z. Liu, Y. Li, X. X. Su, X. Y. Jiao, X. Wang and B. Tang, Mitochondrial peroxynitrite mediation of anthracycline-induced cardiotoxicity as visualized by a two-photon near-infrared fluorescent probe, *Anal. Chem.*, 2018, **90**, 11629–11635.
26 X. Li, M. Tian, G. Zhang, R. Zhang, R. Feng, L. Guo, X. Yu, N. Zhao and X. He, Spatially dependent fluorescent probe for detecting different situations of mitochondrial membrane potential conveniently and efficiently, *Anal. Chem.*, 2017, **89**, 3335–3344.
27 H. Li, C. Q. Xin, G. B. Zhang, X. S. Han, W. J. Qin, C. W. Zhang, C. M. Yu, S. Jing, L. Li and W. Huang, A mitochondria-targeted two-photon fluorogenic probe for the dual-imaging of viscosity and H_2O_2 levels in Parkinson's disease models, *J. Mater. Chem. B*, 2019, **7**, 4243–4251.
28 M. Luan, J. Chang, W. Pan, Y. Chen, N. Li and B. Tang, Simultaneous Fluorescence visualization of epithelial-mesenchymal transition and apoptosis processes in tumor

cells for evaluating the impact of epithelial-mesenchymal transition on drug efficacy, *Anal. Chem.*, 2018, **90**, 10951–10957.

29 L. Fan, J. Y. Ge, Q. Zan, X. D. Wang, S. H. Wang, Y. W. Zhang, W. J. Dong, S. M. Shuang and C. Dong, Real-time tracking the mitochondrial membrane potential by a mitochondria-lysosomes migration fluorescent probe with NIR-emissive AIE characteristics, *Sens. Actuators, B*, 2021, **327**, 128929.

30 J. Luo, Z. Xie, J. W. Y. Lam, L. Cheng, H. Chen, C. Qiu, H. S. Kwok, X. Zhan, Y. Liu, D. Zhu and B. Z. Tang, Aggregation-induced emission of 1-methyl-1,2,3,4,5-pentaphenylsilole, *Chem. Commun.*, 2001, 1740–1743.

31 R. T. K. Kwok, C. W. T. Leung, J. W. T. Lam and B. Z. Tang, Biosensing by luminogens with aggregation-induced emission characteristics, *Chem. Soc. Rev.*, 2015, **44**, 4228–4238.

32 Y. B. Zhou, J. Hua, B. Z. Tang and Y. H. Tang, AIEgens in cell-based multiplex fluorescence imaging, *Sci. China: Chem.*, 2019, **10**, 1312–1332.

33 B. Z. Tang, Z. Zhao, H. K. Zhang and J. W. Y. Lam, Aggregation-induced emission: new vistas at aggregate level, *Angew. Chem., Int. Ed.*, 2020, **59**, 9888–9907.

34 J. Shi, Y. Li, Q. Li and Z. Li, Enzyme-responsive bioprobes based on the mechanism of aggregation-induced emission, *ACS Appl. Mater. Interfaces*, 2018, **10**, 12278–12294.

35 R. Y. Zhang, G. L. Niu, Z. Y. Liu, J. H. C. Chau, H. F. Su, M. M. S. Lee, Y. Gu, R. T. K. Kwok, J. W. Y. Lam and B. Z. Tang, Single AIEgen for multiple tasks: imaging of dual organelles and evaluation of cell viability, *Biomaterials*, 2020, **242**, 119924.

36 M. M. Kang, Z. J. Zhang, N. Song, M. Li, P. P. Sun, X. H. Chen, D. Wang and B. Z. Tang, Aggregation-enhanced theranostics: AIE sparkles in biomedical field, *Aggregate*, 2020, **1**, 80–106.

37 D. Wang, M. M. S. Lee, G. Shan, R. T. K. Kwok, J. W. Y. Lam, H. Su, Y. Cai and B. Z. Tang, Highly efficient photosensitizers with far-red/near-infrared aggregation-induced emission for in vitro and in vivo cancer theranostics, *Adv. Mater.*, 2018, **30**, 1802105.

38 Q. Wu, Y. M. Li, Y. Li, D. Wang and B. Z. Tang, Hydrogen peroxide-responsive AIE probe for imaging-guided organelle targeting and photodynamic cancer cell ablation, *Mater. Chem. Front.*, 2021, **5**, 3489–3496.

39 G. Y. Jiang, C. B. Li, X. Liu, Q. Q. Chen, X. K. Li, X. G. Gu, P. F. Zhang, Q. F. Lai and J. G. Wang, Lipid droplet-targetable fluorescence guided photodynamic therapy of cancer cells with an activatable AIE-active fluorescent probe for hydrogen peroxide, *Adv. Opt. Mater.*, 2020, **8**, 2001119.

40 J. B. Zhuang, N. Li, Y. Y. Zhang, B. L. Li, H. Q. Wen, X. C. Zhang and T. Y. Zhang, Na Zhao and B. Z. Tang. Esterase-Activated Theranostic Prodrug for Dual Organelles-Targeted Imaging and Synergetic Chemo-Photodynamic Cancer Therapy, *CCS Chem.*, 2021, **3**, 1964–1979.

41 X. D. Wang, L. Fan, S. H. Wang, Y. W. Zhang, F. Li, Q. Zan, W. J. Lu, S. M. Shuang and C. Dong, Real-time monitoring mitochondrial viscosity during mitophagy using a mitochondria-immobilized near-infrared aggregation-induced emission probe, *Anal. Chem.*, 2021, **93**, 3241–3249.

42 Y. B. Lai, T. T. Zhang, W. H. Song, Z. H. Li and W. Y. Lin, Evaluation of Cell Viability with a Single Fluorescent Probe Based on Two Kinds of Fluorescence Signal Modes, *Anal. Chem.*, 2021, **93**, 12487–12493, DOI: 10.1021/acs.analchem.1c02911.

43 L. Fan, X. D. Wang, Q. Zan, L. F. Fan, F. Li, Y. M. Yang, C. H. Zhang, S. M. Shuang and C. Dong, Lipid droplet-specific fluorescent probe for in vivo visualization of polarity in fatty liver, inflammation, and cancer models, *Anal. Chem.*, 2021, **93**, 8019–8026.

44 D. Wang, H. F. Su, R. T. K. Kwok, X. L. Hu, H. Zou, Q. X. Luo, M. M. S. Lee, W. H. Xu, J. W. Y. Lam and B. Z. Tang, Rational design of a water-soluble NIR AIEgen, and its application in ultrafast wash-free cellular imaging and photodynamic cancer cell ablation, *Chem. Sci.*, 2018, **9**, 3685–3693.

45 G. Feng, G. Q. Zhang and D. Ding, Design of superior phototheranostic agents guided by Jablonski diagrams, *Chem. Soc. Rev.*, 2020, **49**, 8179–8234.

46 S. Xu, Y. Duan and B. Liu, Precise molecular design for high-performance luminogens with aggregation-induced emission, *Adv. Mater.*, 2020, **32**, 1903530.

